NONDESTRUCTIVE TESTING AND EVALUATION
2023, VOL. 38, NO. 3, 456–479
https://doi.org/10.1080/10589759.2022.2123481

Taylor & Francis
Taylor & Francis Group

Nonlinear ultrasonic characteristics of a corroded steel plate

Markus Nilsson, Peter Ulriksen and Nils Rydén

Division of Engineering Geology, Department of Biomedical Engineering, Lund University, Lund, Sweden

ABSTRACT

Corrosion in leak-tight plate structures, such as the containment liner in Nuclear Power Plants (NPPs), is detrimental to their operational state. To tackle this issue, the present work aims to assess the feasibility of using nonlinear ultrasound to detect corrosion. The corrosion product of main concern in the present study contains several microscopic and macroscopic cracks and delaminations. Three parameters based on nonlinear acoustics were studied by using two types of measurements on a uniformly corroded steel plate. The relative parameter of quadratic nonlinearity (β'), given by the ratio between the second harmonic amplitude and the fundamental amplitude squared, was measured using indexed measurements with a pitch-catch setup while the specimen was immersed in water. The sideband peak count (SPC), which is a measure of the number of sidebands generated from a wide band excitation, was extracted from through-transmission measurements. The third parameter studied is a measure of the energy distributed in the sidebands over the energy at the excitation frequencies (α). This parameter is determined for the same datasets used for SPC. All three parameters increased in the severely corroded region of the inspected steel plate, indicating the potential use of nonlinear ultrasonics to detect corrosion.

ARTICLE HISTORY
Received 22 June 2022
Accepted 31 August 2022

KEYWORDS
Corrosion; delamination; acoustic nonlinearity parameters; ultrasound; non-destructive testing

1. Introduction

Nuclear power plants (NPPs) provide a significant portion of electricity in our societies. In Sweden, about 30% of the electricity comes from nuclear power [1]. The reactor containment buildings usually consist of one thick heavily reinforced concrete wall, shielding the reactor from an external threat, and a leak-tight steel plate construction called a containment liner plate (CLP) [2,3]. The purpose of the CLP is to stop radioactive particles from contaminating the surrounding environment if an accident occurs. The CLP typically consists of 6–10-mm-thick pressure vessel quality steel plates. CLP inspection can normally be done by visual inspection [2], thermography [4], and conventional thickness gauging using ultrasound. However, in certain NPPs the CLP is embedded in concrete, thus making it inaccessible which makes Non-Destructive Testing (NDT) of the CLP very challenging.

Due to the global impact of corrosion damage, multiple ways have been devised to inspect different structures for corrosion. For structures that may suffer from corrosion

CONTACT Markus Nilsson Markus.nilsson@tg.lth.se

damage beneath their accessible surface, for example concrete structures, proposed methods of inspection include electromagnetic methods such as radar [5] and X-ray [6], and acoustical methods such as acoustic emission [7], guided wave testing [8] and ultrasonics [9]. Metal plates are conventionally manufactured by rolling, a metalworking process that relies on passing the material through a series of rolls to reduce the thickness of the material. This process is assumed to form surface-plane parallel internal structures in the plate. When the steel plate then corrodes, such layers are separated, thus creating delaminations and cracks, as seen in Figure 1. Structurally inhomogeneous media, such as metals containing cracks, are known to exhibit strong nonlinear phenomena when excited by elastic waves [10]. In cracked or delaminated media, elastic nonlinearity is caused by effects such as stress concentration at crack tips [11], and stiffness asymmetry (bi-modular elasticity) [12]. Acoustically nonlinear phenomena include the generation of new spectral components in the received acoustic signal. The most commonly studied components are the generation of higher-harmonics and modulation frequencies [13]. Studies into the detection of corrosion-based defects using nonlinear acoustical methods have largely focused on detecting stress corrosion cracking [14–16], intergranular corrosion [17,18], and cracks in concrete structures due to rebar corrosion [19–22]. As shown, several studies into the degradation of reinforced concrete due to rebar corrosion have been carried out. These studies have established that concrete may crack due to embedded elements corroding, and that this cracking can be detected effectively by using nonlinear ultrasonics. However, these studies does not study the nonlinearity of the corroded elements themselves. Instead, the focus is put on the elastic nonlinearity caused by micro-cracks in the surrounding concrete. As this has evidently already been studied extensively, the present work aims to take a different approach.

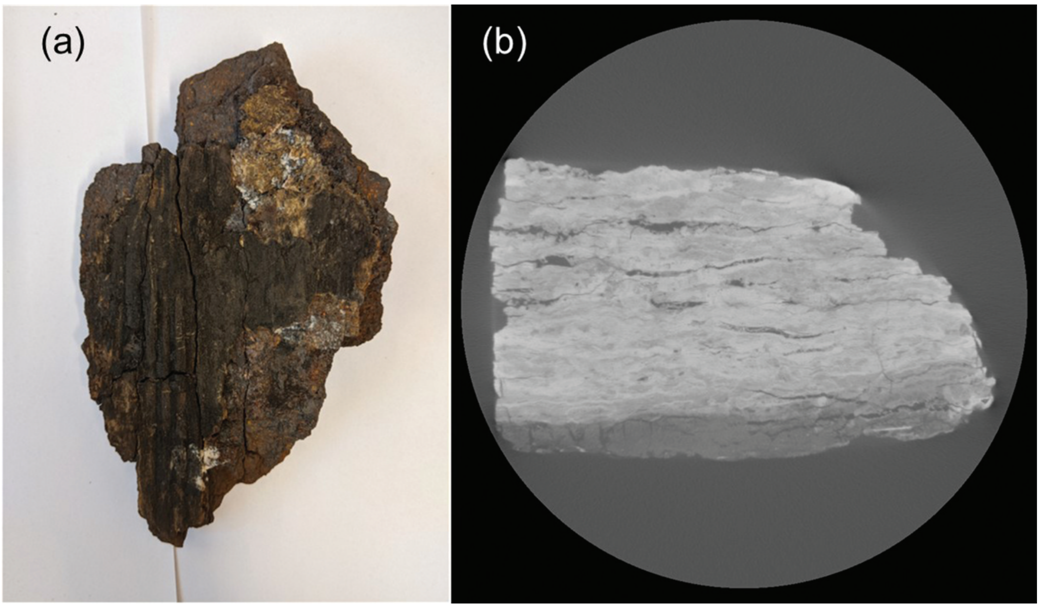

Figure 1. (a) Embedded CLP corrosion product. (b) X-ray tomography showing the cross-section of a piece of the corrosion product shown in (a).

An embedded CLP corrosion product is shown along with X-ray tomography of the corrosion product. The tomography reveals several cracks and delaminations in the cross-section of the corrosion product.

Studies into the detection of general corrosion, also called uniform corrosion [23], using nonlinear acoustical methods are lacking. Uniform corrosion rarely leads to failure and is easily detected visually, which is likely part of the reason why there is a lack of studies on the matter. However, if detection of corrosion attacks at early stages in inaccessible structures is sought, then the detection of gross uniform corrosion must be considered. This is particularly important for structures such as the CLP where the loss of leak tightness is detrimental to the surrounding environment. This study aims to investigate the plausibility of using nonlinear acoustical methods to detect such gross corrosion. Due to the heterogeneity of concrete, it must first be established that corrosion induces significant acoustical nonlinearity on its own before any meaningful conclusions can be drawn from inspection of embedded specimens. This is important because it is not certain that corrosion of plate-like structures embedded in concrete will induce micro-cracking in the concrete. The present work employs two different experimental methods based on probing effects from elastic nonlinearity. To assess the feasibility of using a pitch-catch setup to inspect embedded specimens, the relative parameter of quadratic nonlinearity (β') is measured in an immersed plate using a pitch-catch configuration. The specimen is immersed in water to ensure uniform coupling. The pitch-catch setup is chosen because it is probable that only the inner (or outer) containment wall will be accessible for CLP inspection. It is therefore unlikely that through-transmission will be applicable due to accessibility issues. However, through-transmission measurements can be used to complement the pitch-catch experiment. By applying the Sideband Peak Count (SPC) method [24] in through-transmission experiments, we ensure that energy is transmitted through the corrosion, thus exciting the defects within. The SPC technique relies on using a single wide band excitation to produce and probe intermodulation frequencies, that is, sidebands. Two parameters related to acoustic nonlinearity can be extracted from SPC measurements. These are the SPC itself, which is a measure of the number of sidebands generated, and the nonlinearity parameter α, which is a measure of the energy contained in the sidebands relative to the energy at the excitation components [22].

This study shows that severe uniform corrosion can create crack-like defects (such as delaminations) in the corrosion products. The corrosion also induces severe surface roughness that may affect the measured nonlinearity. Our experiments show that the three parameters of nonlinearity we have studied increase in the severely corroded region of the inspected plate. This indicates that the corrosion-induced defects yield a local increase in elastic nonlinearity.

2. Parameters of acoustic nonlinearity

Conventional ultrasonic methods used for NDT operate on the assumption that linear approximations of the stress–strain relationship hold [25, Ch. 1] due to sufficiently weak excitations. Then, higher-order terms in the governing differential equations can be ignored. However, research has shown that defects such as cracks [26], delaminations [12], and corrosion [17], locally affect the elastic properties to such an extent that this assumption no longer holds, even for low excitation levels. It is well known that crack tips induce stress concentrations that cause acoustic excitations to be locally amplified by several orders of magnitude, thus causing an increase in acoustical nonlinearity [11]. It is also known that cracks cause stiffness asymmetry in their region as the tensile half-periods of an acoustic excitation will force the crack walls apart, thus weakening the region [12]. Nonlinear acoustical methods for NDT have shown great applicability to monitor progressive damage [27]. However, when cracks grow from microscopic to macroscopic, the measured nonlinearity has been shown to decrease in some instances [28]. This could render some difficulty in detecting gross damage using methods based on probing the effects of elastic nonlinearity.

2.1. Extraction of the relative parameter of quadratic elastic nonlinearity

A simple representation of a nonlinear approximation of a stress–strain relationship that includes classical quadratic nonlinearity can be formulated in terms of Hooke's Law in one-dimension [29]:

$$\sigma(\in) = E(\in + \beta\in^2 + \ldots) \tag{1}$$

where σ is stress; $\in$ is strain; E is the linear elastic modulus; and β is the quadratic parameters of nonlinearity. To examine the differences in material nonlinearity between a pristine specimen and a damaged specimen, β can be used. For longitudinal waves travelling in a solid, β is given by Equation (2) [30], where A_i denotes the displacement amplitude for harmonic component i; x is the propagation distance; $k = f\frac{2\pi}{c}$ is the wave number, where f is the fundamental wave frequency; and c is the sound velocity in the inspected medium. For water, it has been shown [31] that a similar expression, which is half of Equation (2), holds.

$$\beta = \frac{8A_2}{A_1^2 k^2 x} \tag{2}$$

If the transfer functions of the transducers used are not known, then it might be cumbersome to translate the voltage signal into displacement, making it difficult to determine the true parameter of quadratic nonlinearity. In such cases, it might be advantageous to determine the relative parameter of quadratic nonlinearity instead. Given that displacement is proportional to the received voltage signal amplitude, the true quadratic parameter must be proportional to the ratio of the second harmonic amplitude and the fundamental component squared, as given by Equation (3) [13, Ch. 2.2]. When comparing parameter values between different measurements, it is important to either use the same transmitter/receiver pair, or be aware of the acoustic-electric transfer function absolute values at the first and second harmonic for the transducers used. Not adjusting for sensitivity differences could yield erroneous comparisons.

$$\beta \propto \frac{A'_2}{{A'_1}^2} = \beta' \tag{3}$$

Here, $'$ indicates the usage of the measured voltage signal amplitude of the fundamental and second harmonic extracted from the magnitude spectrum of the received signal. As indicated by Equation (2), the parameter does not only vary with displacement amplitudes but varies also with the propagation distance and the wavelength. It is therefore important to maintain a fixed propagation distance and as similar a wavelength as possible during experiments. Assuming that the frequency is fixed, it is important to note any differences in the sound velocity in each respective specimen. Not correcting for differences might yield erroneous conclusions when comparing parameter values. If the propagation distances in the inspected specimens are not held constant, for example when a plate with varying thickness is inspected, a correction factor must be applied when comparing parameter values. Assuming that the plate has a uniform sound velocity (wave number held constant), then a correction factor can be applied to the areas with differing thickness with respect to a reference thickness x_0. If Equation (2) is studied, it is evident that a large x-value (here plate thickness) will render the lowest β-value. By choosing $x_0 = x_{max}$, this relation is maintained. The corrected β' is then given by Equation (4) where i is the measurement point notation:

$$\beta'_{corr} = \frac{x_{max}}{x_i}\beta'_i = K_i\beta'_i \tag{4}$$

To ensure that the parameters have been measured successfully one of the three input variables can be varied, as discussed extensively in Ref [13, Ch. 2.3.4]. As propagation distance and wave number might be difficult to vary in a controlled manner, varying the excitation amplitude is recommended. For example, if β' is measured successfully, A'_2 should increase linearly with A'^2_1, as seen from Equation (3). The values of the relative quadratic parameter in a measurement point can be extracted by fitting a line to the acquired data points. The slope of the regression line will yield the relative parameter value ($A'_2 = A'^2_1\beta' + m$) as an average of the input amplitudes, given that the correlation coefficient R^2 is high, indicating a good fit. Ideally, the intercept term in the regression-line formulation should be equal to zero, but due to parasitic nonlinearity from the electrical equipment, some offset is expected.

2.2. Sideband peak count

When a structure is subjected to a transient excitation, a wide band of frequency components is excited. If the medium that is being excited is strongly scattering and/or nonlinear, the frequency components contained in the transient will start to interact, thus generating intermodulation components, that is, sidebands. For rigorous mathematical derivations of the generation of modulation components, the reader is referred to Refs [24,32,33]. The Sideband Peak Count (SPC) is defined as the number of sideband peaks above a threshold governed by the weakest dominant peak [32] (Equation (5)). Let the weakest dominant peak be 0.1 times the strongest peak (1 in the normalised spectrum). The sidebands are then assumed to be weaker than 0.1, thus the threshold maximum would be undefined.1. The SPC is defined as the ratio of peaks in the normalised frequency spectrum above the moving threshold ($N(th)$) over the total number of peaks (N_{tot}) greater than the noise level but weaker than the dominant peaks. An illustration of the modulation phenomenon and the SPC method is shown in Figure 2. Here, the excitation is illustrated as having three dominant peaks. When interacting with a linear medium, these are the only frequencies present in the spectrum ((a) in Figure 2). In the nonlinear medium ((b) in Figure 2), the three dominant peaks interact which

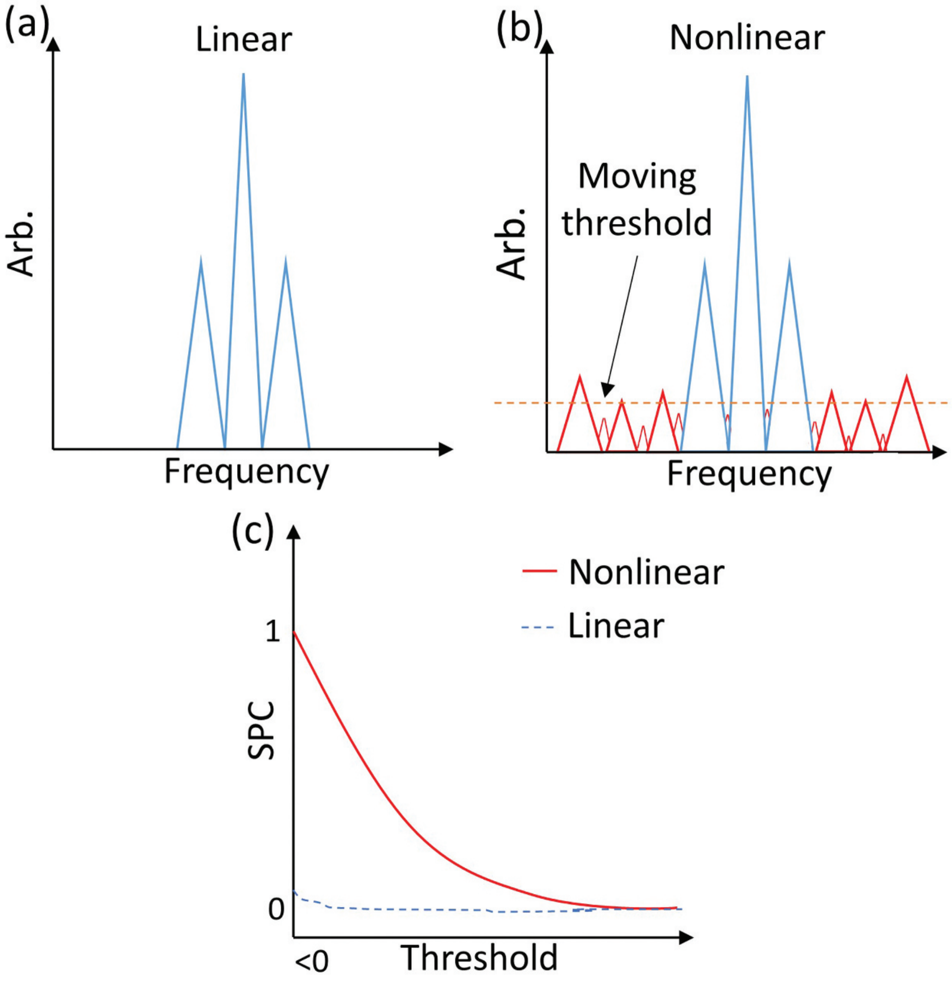

Figure 2. Illustration of the Sideband Peak Count method. (a) a linear response only contains the excitation frequencies, i.E. dominant peaks (blue). (b) the nonlinear response contains the dominant peaks, as well as sidebands generated by intermodulation of the excitation frequencies and nonlinear components (red). (c) the SPC is defined as the ratio between the number of peaks above a moving threshold over the total number of peaks. The SPC approaches zero as the threshold value increases. When a linear medium is excited by a wideband excitation, only the excitation frequencies, that is, dominant peaks, are represented in the frequency spectrum. Here indicated by three peaks. When a nonlinear medium is excited in a similar fashion, additional frequency components are generated, so-called sidebands. In addition to the three dominant peaks, the frequency spectrum now contains several sideband peaks. The sideband peak count (SPC) is a measure of the number of sideband peaks whose magnitudes are greater than some threshold value. At low threshold values, the SPC is greatest, and the SPC will gradually decrease as the threshold value increases.

generates intermodulation components, that is, sidebands. As the wave propagates, the nonlinear effects accumulate and more nonlinear interactions arise, thus generating more sidebands. The moving threshold will then start at some value >0 and move towards the maximum threshold value, which is given by the weakest dominant peak. At the lowest threshold value, the number of sideband peaks will be the greatest which means that the SPC will start at 1 for the measurement acting as reference. In Figure 2(c) this would be the nonlinear case. As the threshold increases, the SPC will decrease and approach zero, which is illustrated in Figure 2(c). Observe that the illustration in Figure 2(c) shows non-zero SPC for the linear case at low threshold values. This is because there is always some nonlinearity to be expected, even in pristine specimens due to inherent atomic nonlinearity and/or parasitic nonlinearity from the electrical equipment. Note that the dominant peaks are excluded in the SPC, which means that peaks above the maximum threshold will be ignored in the computation.

$$SPC(th) = \frac{N(th)}{N_{tot}} \tag{5}$$

The number of sidebands grows with increasing nonlinearity, but it may be advantageous to compare the energy distributed in the sidebands rather than the number of sidebands. There is always some inherent nonlinearity to be expected due to weak atomic nonlinearity and parasite nonlinearity from the equipment used, and thus, some sidebands will be generated. The authors of [22] proposed a nonlinearity parameter α based on work from [34] that is defined as the energy contained in the nonlinear components, that is, sidebands (W_{NL}), over the linear components, that is, the excitation frequencies (W_L), as given by Equation (6). The energy is conventionally given by the integral of the squared magnitude, but such integrals would also contain energy from noise. The possible impact from noise can be reduced by instead of using the conventional energy, using the sum of the magnitudes of the linear components as W_L, and the sum of magnitudes of the nonlinear components as W_{NL}. Henceforth, the term energy will therefore be used interchangeably with magnitude. This measure of energy distribution is likely more sensitive to structural damage than the SPC as the generation of sideband components might be saturated, meaning that no additional sidebands are detected with increased nonlinearity. However, the increased energy distributed from the fundamental components to the sidebands yields greater magnitudes at these peaks, thus greater α. This is particularly important for experimental considerations as transducers have limited bandwidth, and are therefore only capable of adequately detecting sidebands in a limited frequency band.

$$\alpha = \frac{W_{NL}}{W_L} \tag{6}$$

3. Experimental investigation

3.1. Inspected specimen

The plate inspected in the present work (see Figure 3) was composed of ordinary construction steel and had the approximate dimensions $225 \times 260x8$ mm. Initially, it was uniformly sheet corroded over its entire surface, but the sheet corrosion was separated from the plate during handling. A piece of the top sheet corrosion layer with approximate dimensions $90 \times 115x2$ mm was reattached to the plate by gluing it using superglue (ethyl 2-cyanoacrylate). Before being glued, the corrosion shell was painted with water-resistant varnish to avoid the dissolution of the corrosion product when immersed in water. The glue was spread evenly across the contact area of the corrosion shell before the shell was placed on the corroded side of the plate (see Figure 3). Gluing likely affects the contact-coupling in the region, as it might induce air bubbles and other inhomogeneities. The corrosion shell was included because, upon an investigation of other pieces of the corrosion product, a large number of delaminations of varying sizes were found. Optical microscopy using a Keyence

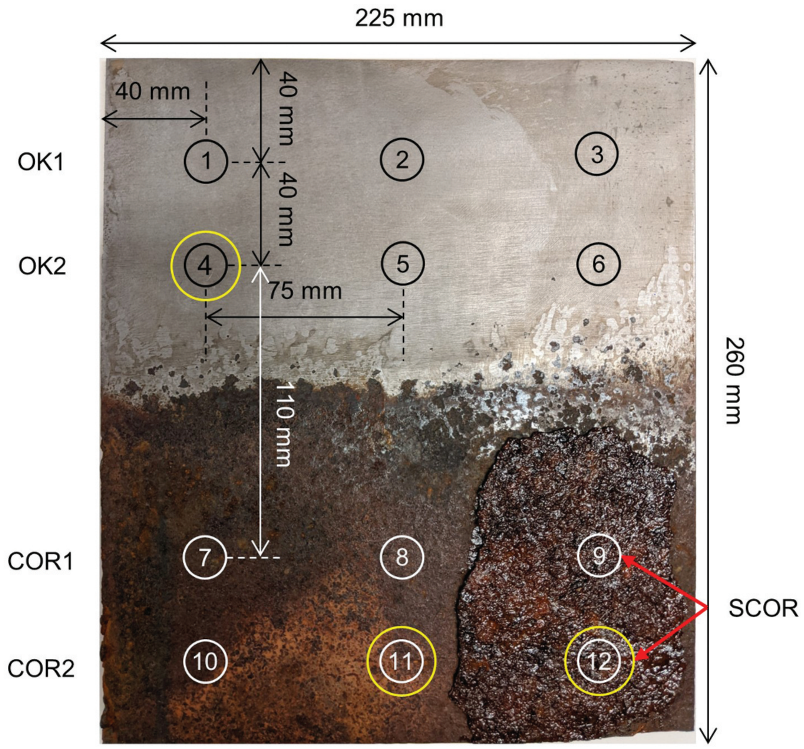

Figure 3. The steel plate used in the present work. Half of the plate was ground with a belt grinder to remove the top corrosion layer. This area is called OK and contains two measurement rows with three measurement points each (OK #1 - #6). The uniformly corroded area is called COR with a measurement point notation of COR #7, #8, #10, and #11. The third area contains the shell-type corrosion product and is denoted SCOR with measurement points SCOR #9 and #12. Data for measurement points highlighted with yellow circles are presented in Figures 8–10 and are used for the SPC measurements presented in Section 4.2.

A steel plate with three distinct regions, one from which corrosion has been removed by means of belt grinding. One uniformly corroded region which is about two-thirds in size of the non-corroded region. The third region is uniformly corroded and contains a reattached corrosion shell. The size of this area is a third of the non-corroded region.

VHX-6000 revealed several surface cracks and delaminations in the bulk of the corrosion shell (Figure 4). X-ray tomography (Figure 5) of a piece of corrosion shell with dimensions 15 × 15x2 *mm* was conducted at the 4D-imaging lab at the division of Solid Mechanics at Lund University using a Zeiss Xradia XRM520 with 13 resolution. The tomography revealed delaminations and cracks in the micro- to macro-scale throughout the cross-section of the corrosion product (Figure 5). Similar delamination characteristics have been found in other corrosion products, as seen in Figure 1 and Refs [35–37]. It is suspected that this delamination characteristic can be found in most corrosion products that are severe enough to be of interest to detect, which makes it interesting to study the feasibility of using nonlinear ultrasound to detect them.

The uniform corrosion on the surface of half the plate area was removed by using a belt grinder to ensure that the only property changes in the plate were due to corrosion. This allowed the plate to have an area deemed undamaged. Due to the grinding and corrosion, the plate had varying thicknesses (6.13–8.67 mm). Table 1 shows the thicknesses at the measurement points as determined using a caliper. The values in

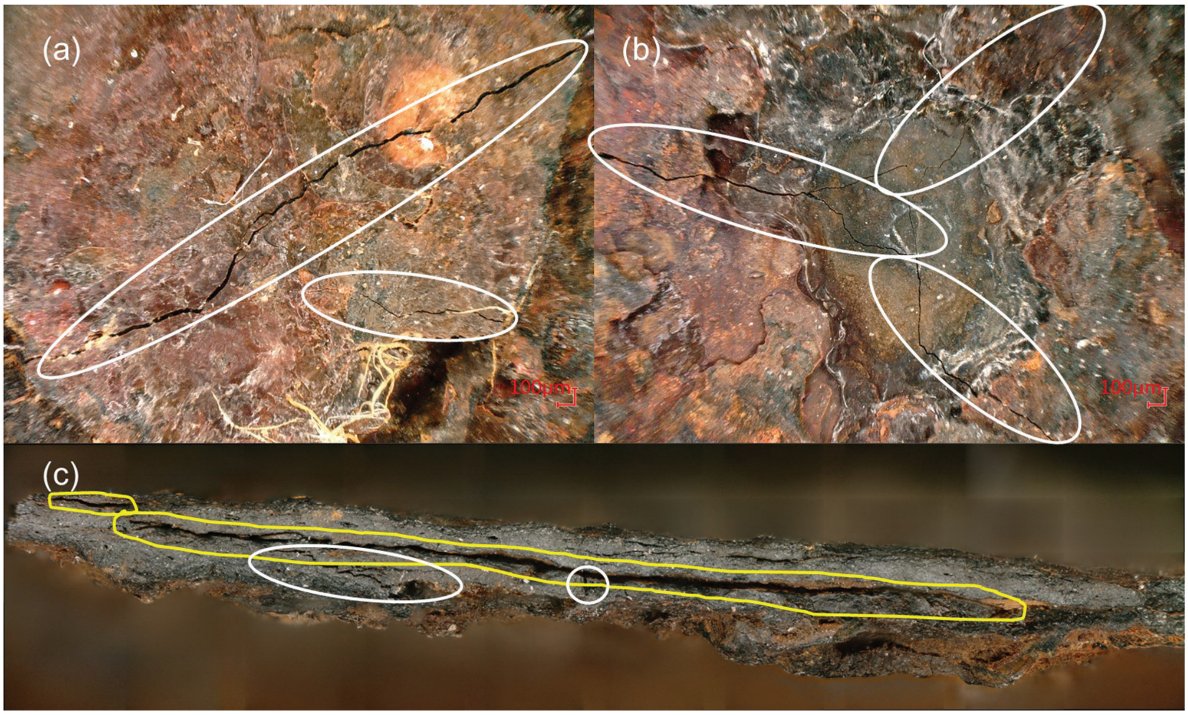

Figure 4. Optical microscopy (Keyence VHX-6000) of a corrosion shell. (a), (b) Cracks in the surface of the corrosion product indicated by white circles. (c) Stitching of several images acquired over the bulk of the corrosion product, indicating severe delaminations (yellow markings) and several cracks (white circles).
Several cracks are noticed on the surface of a sheet corrosion product. The corrosion product also contains delaminations seen in the bulk of the corrosion product.

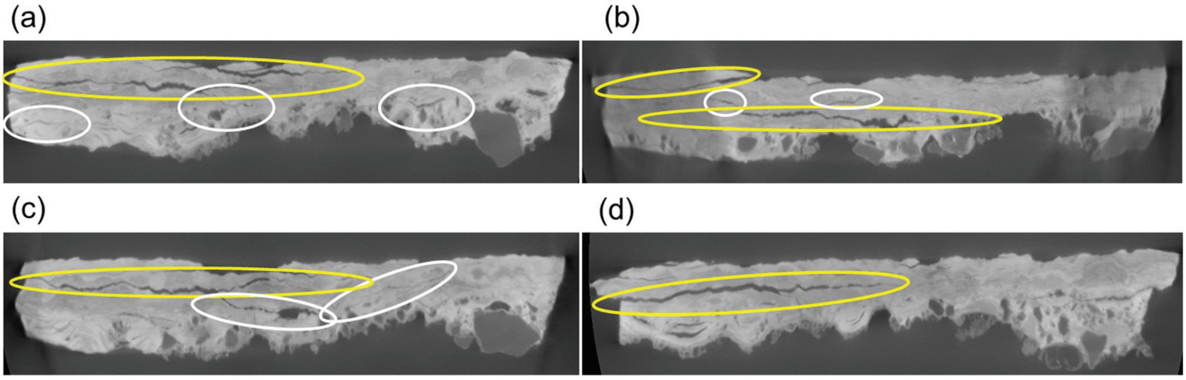

Figure 5. X-Ray tomography showing several delaminations (yellow circles) in the cross-section of a small piece of a corrosion shell. (a) Two clearly visible delaminations and several less visible cracks (white circles). (b) Two large delaminations and several cracks. (c) One large and one less severe delamination. (d) a delamination that is almost perfectly parallel with the surface plane of the corrosion product.
X-ray tomography reveals several cracks and delaminations in the cross-section of a sheet corrosion product.

parentheses are the measured thicknesses before attaching the corrosion shell. Points 5 and 8 were not possible to reach with the caliper, therefore, the thicknesses at these points were estimated by taking an average of the points next to them, that is, points 4 and 6 for

Table 1. Plate thickness at the measurement points.

Measurement point (#)	Plate thickness x_i (mm)
1	6.13
2	6.29
3	7.28
4	7.08
5	*7.36*
6	7.63
7	8.28
8	*8.30*
9	10.7 (8.32)
10	8.62
11	8.67
12	**11.0** (8.53)

point 5 and points 7 and 9 (before the corrosion shell) for point 8. The sound velocity was estimated to be undefined 000 m/s in all regions of the plate. This measurement used a Lecoeur US-key USB ultrasound device coupled with a 5 MHz transducer (Olympus M1042) in a pulse-echo configuration, using the same transducer as a receiver. It is likely that the measured sound velocity is only valid for the bulk of the material and that local velocity variations would occur in the corroded volume.

Since the severity of corrosion-induced damage might vary over the corroded area, the inspection was performed at several measurement points. As can be seen in Figure 3, the entire inspection area was split into 4 rows, 2 in each area of interest, with a total of 12 measurement points. The ground area is called OK, hence OK1 and OK2 describe the rows in the plate area without corrosion. The uniformly corroded area is called COR (for corroded), with measurement rows COR1 and COR2. COR also includes the corrosion shell and measurement points associated with the shell are denoted SCOR. Figure 3 shows the spacing between each measurement point using correct scaling; 75 mm in the horizontal direction and 40 mm in the vertical direction between adjacent rows. The spacing between OK2 and COR1 was 110 mm.

3.2. Determining β' using immersed pitch-catch

A schematic for the pitch-catch configuration used in the present work can be seen in Figure 6. A 4.5 MHz sine-burst with four cycles was generated by an Agilent 33250A waveform generator (AWG). The voltage signal from the AWG was amplified in two steps: first pre-amplified by the Schaffner CBA9425 to reach higher voltage levels than those generated by the AWG, then final amplification using a Xiegu XPA125B amplifier. A total of 6 excitation levels were used: 14, 30, 47, 63, 74, and 80 V_{pp}. Some of these excitation levels could be reached without the two-step amplification. However, the amplification process was kept throughout all measurements to keep potential errors, such as parasitic nonlinearity, constant. The output from the XPA125B amplifier was terminated into a high-power 50 Ω load (Ritec RT50) before the amplified signal was sent to the transmitter. The transmitter was an Olympus V309-SU immersion transducer (**T** in Figure 6) with a centre frequency of 4.5 MHz and a beamwidth (full width at half maximum) of 5 mm measured 130 mm away from the transducer. The number of cycles used was determined by using the thickness of the plate as guidance. The spatial length of the sine-burst must be less than the specimen thickness to avoid generating

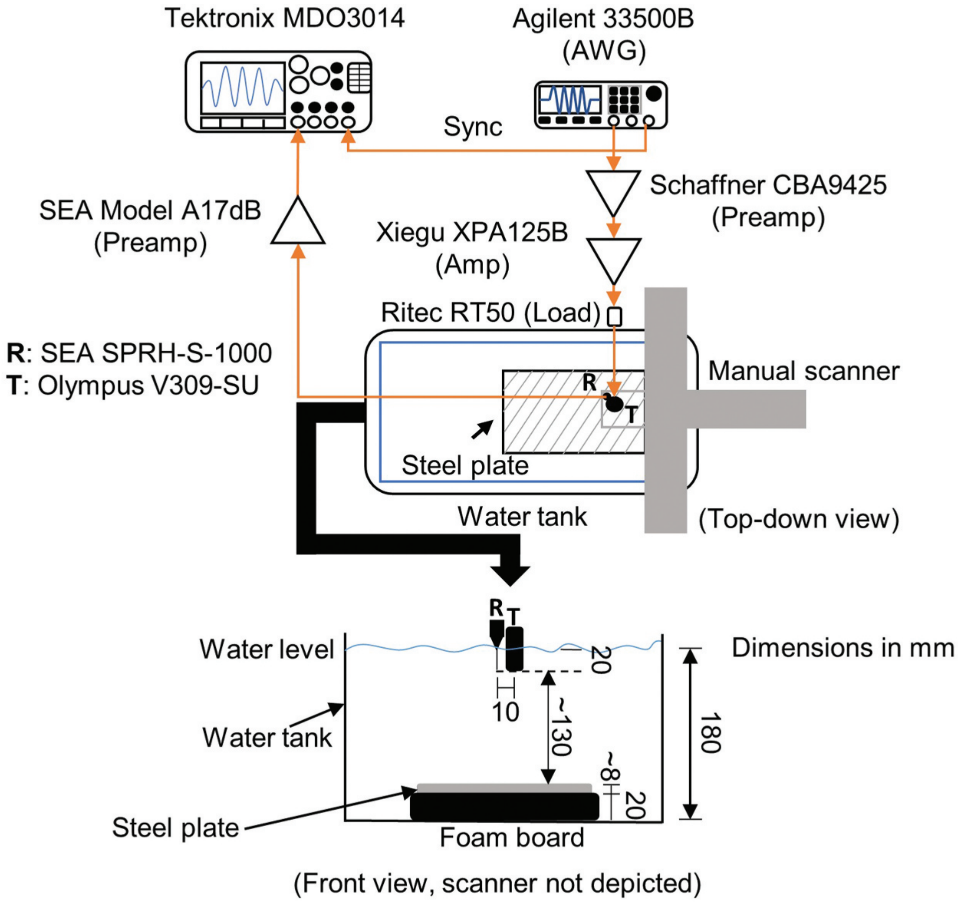

Figure 6. Schematic for the experimental setup used in the reported work.
Decorative schematic of the pitch-catch setup used for the immersion experiment.

spurious harmonics due to interference between incident and reflected waves within the specimen. In the present case, the sound velocity in the bulk material was estimated to be 6000 m/s, which yields a spatial resolution of approximately 5.3 mm for the 4.5 MHz 4-cycle tone-burst. This is less than the thinnest part of the plate (see Table 1). The distance between the plate and the transducer/receiver was kept at approximately 130 mm. As the plate thickness varies, so does this distance. To minimise reflections from the bottom of the water tank, the plate was placed on a 20 mm thick high-density foam board with similar dimensions as the plate. The water temperature was $20 \pm 0.2^{\circ} C$. The reflected wave was received by a SEA SPRH-S-1000 needle hydrophone (**R** in Figure 6) with high sensitivity in the frequency band 1.5 MHz to 10 MHz. This frequency range covers both the fundamental frequency (4.5 MHz) and the second harmonic (9 MHz). The hydrophone was placed next to the transducer with an offset of 10 mm measured from the centre of the transducer. As the measured beam width is half of the offset, it is possible that the setup records side-lobes of the reflected signal. Thus, the recorded second harmonics might be weaker than those if the main lobe was recorded. Given that the placement of the transducers is constant, the error is also constant and should not severely impact the parameter comparison between regions. The transducer and hydrophone were placed approximately 20 mm under the water surface as measured from their faces. This implies a total water level of 180 mm relative to the bottom of the water tank. The received signal was pre-amplified with a SEA Model A17 dB before being acquired by a Tektronix MDO3014 oscilloscope. A sync signal from the AWG was used to trigger the measurement. Each measurement was repeated 16 times for averaging purposes. A manual XY-scanner was used to move the transducer and hydrophone pair to ensure equal and consistent movement of both parts. Post-processing (windowing, DFT, and more) was done on a PC in the MATLAB environment. Measurements were not taken until the plate had been submerged for several minutes to reduce the most immediate effects caused by the effects of thermodynamic perturbation (slow dynamics [38,39]) due to the immersion. The surface of the transducers was carefully wiped with a sponge cloth after moving the transducer-pair to a new point in order to remove any bubbles that may introduce spurious harmonics.

3.3. Through-transmission for SPC

A schematic for the through-transmission setup for the SPC measurements is shown in Figure 7. The steel plate was placed on a foam board resting on a tabletop scissor lift. The purpose of the foam board is to reduce noise from environmental vibrations. A 4.5 MHz 4-cycle Hanning-windowed sine-burst is used to excite the plate which is amplified by a Schaffner CBA9425 amplifier which is terminated by a high-power 50 Ω load (Ritec RT-50). The transmitter (Olympus V309-SU) is pressed to the plate and held by a clamp on a laboratory stand. The receiver (Olympus M1042) is mounted on the plate by magnetic contact. The transducers are coupled to the plate by using ultrasound gel. Both transmitter and receiver have a centre frequency of 4.5 MHz. The received signal is pre-amplified by an HP 8447D Dual pre-amp (25 dB gain) before being collected in an oscilloscope. The data was transferred from the oscilloscope to a PC for post-processing. The SPC measurements were carried out at three points, OK #4, COR #11, and SCOR #12 seen in Figure 3.

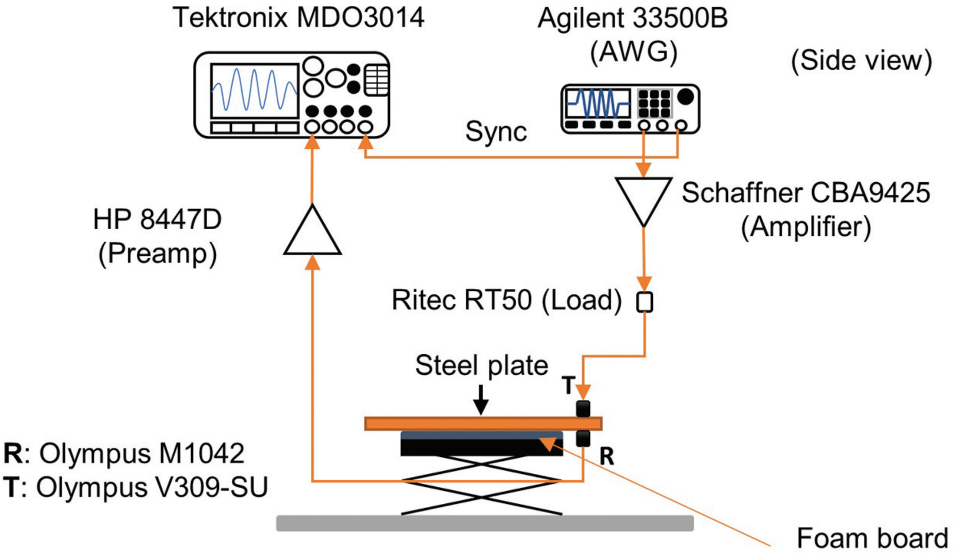

Figure 7. Schematic for the experimental setup used in the SPC measurements (side view). Decorative schematic of the through-transmission experiment.

4. Results and discussion

4.1. Relative quadratic nonlinearity

Figure 8 shows typical time signals at the highest excitation levels for measurement points in each inspected region: OK #4, COR #11, and SCOR #12. The x-markings and vertical dashed lines in the plots indicate the data intervals used for amplitude extraction. The intervals are selected by neglecting the initial and final transient responses to achieve the most stable amplitude level possible for the echo of interest. A steady-state interval would be optimal but would require many more cycles. The time-of-arrival of the echo of interest is estimated by the time-of-arrival for the first echo at region OK, which here is approximately 173.8 μs as seen in Figure 8. As the COR and SCOR regions are both thicker than the OK region, it is expected that echoes from these regions arrive earlier, which is seen in Figure 8. Note that the signals for COR #11 and SCOR #12 both have echoes before the echo of interest. These might originate

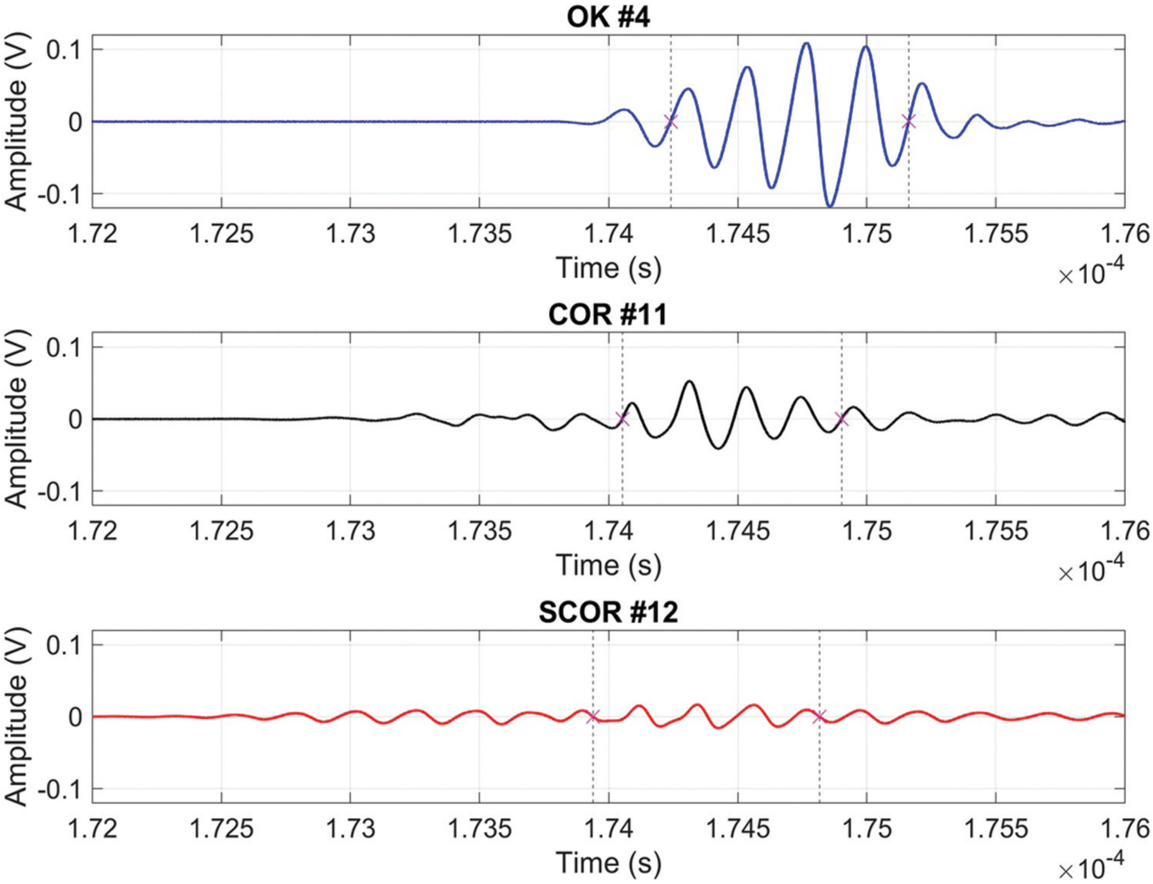

Figure 8. Time signals for measurement points #4 (top, blue line), #11 (middle, black line), and #12 (bottom, red line) at the highest excitation level ($80V_{pp}$). The 'x' markings and vertical dashed lines indicate the intervals extracted for further analysis. Data within these intervals are windowed with a Hanning window before the amplitude spectra are obtained. Note the clear differences in amplitude between the three regions. The inset figures and vertical dashed line show that the time of arrival is slightly faster for the signals collected in the corroded areas.

Time signals represented in voltage versus time plots at measurement points four (OK), eleven (COR), and twelve (SCOR). The intervals extracted for analysis are: OK; one hundred seventy-two and two tenths to one hundred seventy-five and two tenths microseconds. COR; one hundred seventy-four and one tenth to one hundred seventy-four and nine tenths microseconds. SCOR; one hundred seventy-three and nine tenths to one hundred seventy-four and eight tenths microseconds.

from layers in the corroded structure, or they are due to the significant surface roughness in the respective regions. For SCOR #12, likely, the first echo seen in the bottom plot in Figure 8 is caused by the interaction between the glue and corrosion shell. The additional echoes make it difficult to separate successive reflections accurately which in turn makes attenuation correction very challenging. Because of this, no efforts have been made to correct attenuation differences in the regions.

After the data within the marked intervals are extracted, a Hanning window is applied without overlap before amplitude spectra are obtained. The Hanning window is used because it has been shown [13, Ch. 2.4.4] that it causes less intense side-lobes than, for example, the Tukey window does. The magnitude spectra for the time signals in Figure 8 are shown in Figure 9 along with the magnitude spectra for the remaining five excitation levels. The colours represent the six excitation levels as seen in the legend in Figure 9(c). All measurements generated second harmonics. A step-wise attenuation is clearly seen in Figure 9 (a–). The amplitude levels are reduced by more than 50% at each stage of corrosion. The most interesting observation in Figure 9 is the similarity in the second harmonic levels between (b) and (c), corresponding to COR #11 and SCOR #12, respectively. The levels of the second harmonics are almost equal, but the levels of the fundamental components in (c) are less than

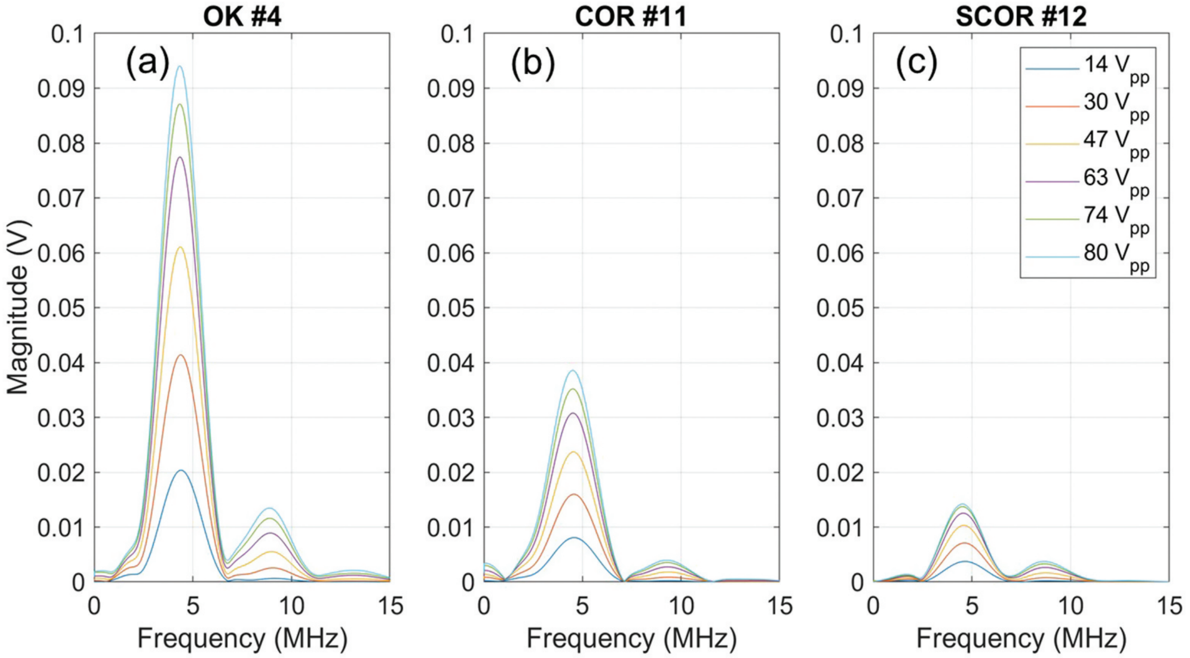

Figure 9. Magnitude spectra obtained at all six excitation levels for the measurement points shown in Figure 8. The spectra corresponding to the time signals shown in Figure 8. are the cyan lines with the highest magnitude. (a) Spectra for measurement point #4 (no corrosion). (b) Spectra for point #11 (uniform corrosion). (c) Spectra for #12 (shell-type corrosion). The amplitude levels decrease at each stage of corrosion. Note the similar level of the second harmonics in (b) and (c), while the level of the fundamental frequency of (c) is less than half of (b). Colours represent the different excitation levels: blue is $14V_{pp}$, orange is $30V_{pp}$, yellow is $47V_{pp}$, purple is $63V_{pp}$, green is $74V_{pp}$, and cyan is $80V_{pp}$.
Magnitude in volts plotted versus frequency for the measurements carried out at points four (OK), eleven (COR), and twelve (SCOR). The maximum magnitude at point four was ninety-four millivolts, and the second harmonic magnitude was thirteen millivolts. At point eleven, the corresponding maximums were approximately thirty-nine and four millivolts respectively. At point twelve the maximum values were fourteen and four millivolts.

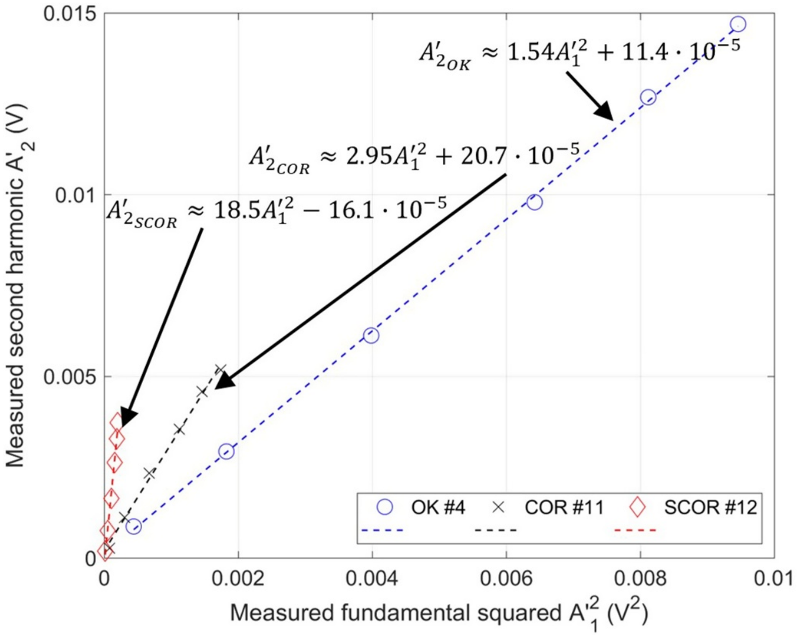

Figure 10. A'_2plotted versus $A'_1{}^2$. Dashed lines are regression lines for the data points (blue circles for #4, black crosses for #11, and red diamonds for #12). The expressions for the regression lines are shown. Note the increase in inclination of the regression lines with increasing grade of corrosion damage.
The magnitudes of the second harmonics for six excitation levels are plotted versus the corresponding magnitude of the fundamental component squared. Data is presented from the measurement points four (OK), eleven (COR), and twelve (SCOR).

half of the corresponding levels in (b). It is also worth mentioning that very clear harmonics are generated for the measurements in OK #4. These could perhaps have been reduced by using a low-pass filter between the XPA125B amplifier and the transmitter, given that the observed harmonics were not generated by small internal defects or inherent atomic nonlinearity.

To determine β', the fundamental (A'_1) and second harmonic (A'_2) amplitudes were extracted from the magnitude spectra as described in Section 2.1. The amplitudes obtained (and squared in the case for A'_1) from the spectra seen in Figure 9 were plotted in Figure 10 along with regression lines fit to the data. By plotting the extracted amplitudes in this manner, the most interesting observation made is the slope of the regression lines. A gradual increase in the slope is seen for increasing grade of corrosion. The slope for OK #4, which is equivalent to β' before the application of correction factor K, is approximately 1.54. The corresponding value is 2.95 for COR #11, and 18.5 for SCOR #12. The computed regression lines for all measurement points have a correlation coefficient (R^2) exceeding 0.99, which indicates a good fit. Table 2 presents β'-values scaled with K given by Eq. ((2.4)). By using $x_{max} = 11.0$ mm (thickness at point #12 from Table 1), the corrected β' for OK #4 is 2.39 ($K_4 = 1.55$) and $\beta'_{11} = 3.74$ ($K_{11} = 1.27$). β'_{12} is still approximately 18.5 as $K_{12} = 1$. The intercept is small and similar for all measurements, which indicates a low level of parasitic nonlinearity from the electrical equipment.

Figure 11(a,b) show A'_1 for all measurement points (refer to Figure 3 for measurement point locations) across the plate and the average A'_1 for each inspected region. The significant difference in attenuation between the three regions is made apparent by plotting the amplitude

Table 2. Thickness correction factors K_i and corrected β' values for all measurement points.

Measurement point (#)	K_i	Corrected β'_i
Region **OK**	-	-
1	1.80	3.08
2	1.75	5.50
3	1.51	3.68
4	1.55	2.39
5	1.49	3.39
6	1.44	1.70
Region **COR & SCOR**	-	-
7	1.33	3.2
8	1.32	2.16
9	1.03	11.7
10	1.28	6.15
11	1.27	3.74
12	1.00	18.5

distribution. Studies of the average A'_1 for each region show that the amplitude levels are reduced by approximately 50% going from OK to COR, and when going from OK to SCOR, the corresponding reduction is 86% on average (72% for COR – SCOR). Granted, there are only two measurement points for SCOR taken into account, which might make the average values less accurate than those for OK and COR, respectively. These results indicate an increase in attenuation with increasing deterioration, which is to be expected as the thickness of the corrosion is largest in this area due to the added corrosion shell. Moreover, it is well-known that corrosion induces significant acoustic attenuation [40]. When studying the levels of A'_2 in Figure 11(c,d) similar contrasts are seen. By looking at A'_2 alone, erroneous conclusions concerning the material state might be drawn if high harmonic amplitudes are assumed to indicate damage. The region with removed corrosion exhibits significantly higher harmonic amplitudes than the corroded region. If β' is studied instead, a similar but inverted contrast is acquired, as indicated by Figure 11(e,f) where the β' values from Table 2 are used. Even if attenuation differences likely also affect the β' values, it would seem that the parameter is sensitive to the damage type induced by the shell-type corrosion product. As indicated by Figures 4 and 5, the shell-type corrosion products likely contain several severe delaminations and cracks, which could explain the vast increase in β'. This result shows the importance of quantifying the nonlinear response in other ways than harmonic amplitudes. Direct use of harmonic imaging for detecting uniform corrosion damage might give false indications of damage in pristine areas of a specimen. This is because the strong attenuation might cause low harmonic levels in the corroded regions. Furthermore, the result also indicates the importance of indexed measurements or scanning techniques to detect corrosion, as single-point measurements might not be sufficient to detect corrosion defects.

It is clear that corrosion induces significant acoustic attenuation, which is likely at least partially due to the diffraction caused by increased surface roughness. The beamwidth in the configuration used in the pitch-catch measurements was 5 mm, which is greater than the diameters of most of the peaks and troughs caused by increased roughness in the corroded regions. When the sound beam hits the surface, it is likely partially scattered, which ultimately leads to a less intense sound wave being recorded by the hydrophone. This would likely not be an issue if the corrosion is embedded in concrete as concrete itself is a heterogeneous material, thus effectively scattering internal vibrations.

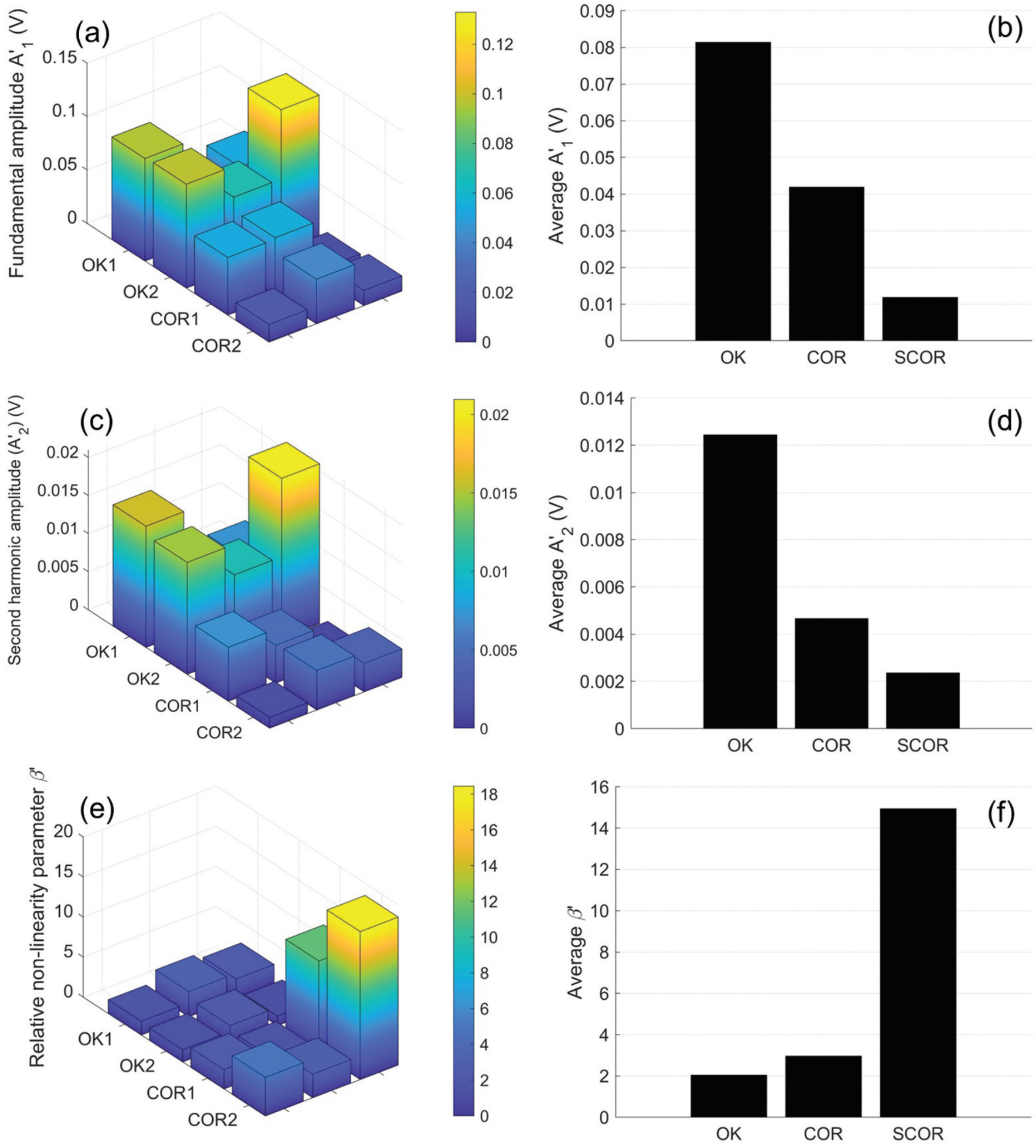

Figure 11. (a) A'_1 levels at the highest excitation level for each measurement point on the plate. A sudden decrease in amplitude level is displayed between the OK and COR regions, with an even more significant decrease in the SCOR area. (b) Average A'_1 at each region. (c) Corresponding A'_2 levels and the clear contrast between OK and COR. (d) the average A'_2 levels. (e) β' values obtained for each measurement point with applied correction factors (values presented in Table 2). The difference between OK and COR is not as significant as in (a) and (c), and no contrast between the two main regions (OK and COR) is observed. However, β' values at the SCOR region clearly stand out from all other measurement points. Refer to Figure 3 for measurement point locations. f) Average β'.

(a) Isometric three-dimensional bar plot of the amplitudes of the fundamental component at each measurement point. (b) Bar plot of the average fundamental amplitudes at regions OK, COR, and SCOR respectively. The levels are approximately eighty-one millivolts at OK, forty-two millivolts at COR, and twelve millivolts at SCOR. (c) Isometric three-dimensional bar plot of the amplitudes of the second harmonics generated at each measurement point. (d) Bar plot of the average second harmonic magnitudes at each measurement region. The levels are approximately twelve millivolts at OK, four and seven tenths of a millivolt at COR, and two and four tenths of a millivolt at SCOR. (e) Isometric three-dimensional bar plot of the β prime distribution. (f) Bar plot showing the average β prime values at each region. The values are three and three tenths at OK, three and eight tenths at COR, and fifteen at SCOR.

Moreover, the offset of the receiver hydrophone might result in side-lobes of the reflected signals being recorded. This could affect the recorded harmonic levels, as they are expected to be highest in the main lobe. The surface roughness in the corroded region and the small slopes in the ground area (OK) likely also affects the measurements as it induces mode conversion. The experimental setup could be further optimised by using a low-pass filter before the transmitter to reduce parasite nonlinearities originating from the electronics, and by using a broadband transducer capable of both acting as transmitter and receiver with adequate sensitivity at the second harmonic.

4.2. Sideband peak count and a

The received signals from the transmission measurements in points OK#4, COR#11, and SCOR#12 are shown in Figure 12. By simply looking at the signals, it is evident that SCOR induces greater self-interaction than at the other two measurement points. This is likely caused by reflections in the top corrosion layer and these reflections cause challenges if echoes were to be separated for accurate attenuation correction. Because of this, efforts towards attenuation correction are not made.

To determine the number of sideband peaks for each measurement, the magnitude spectrum is computed over the entire time signal with a rectangular window. The spectra

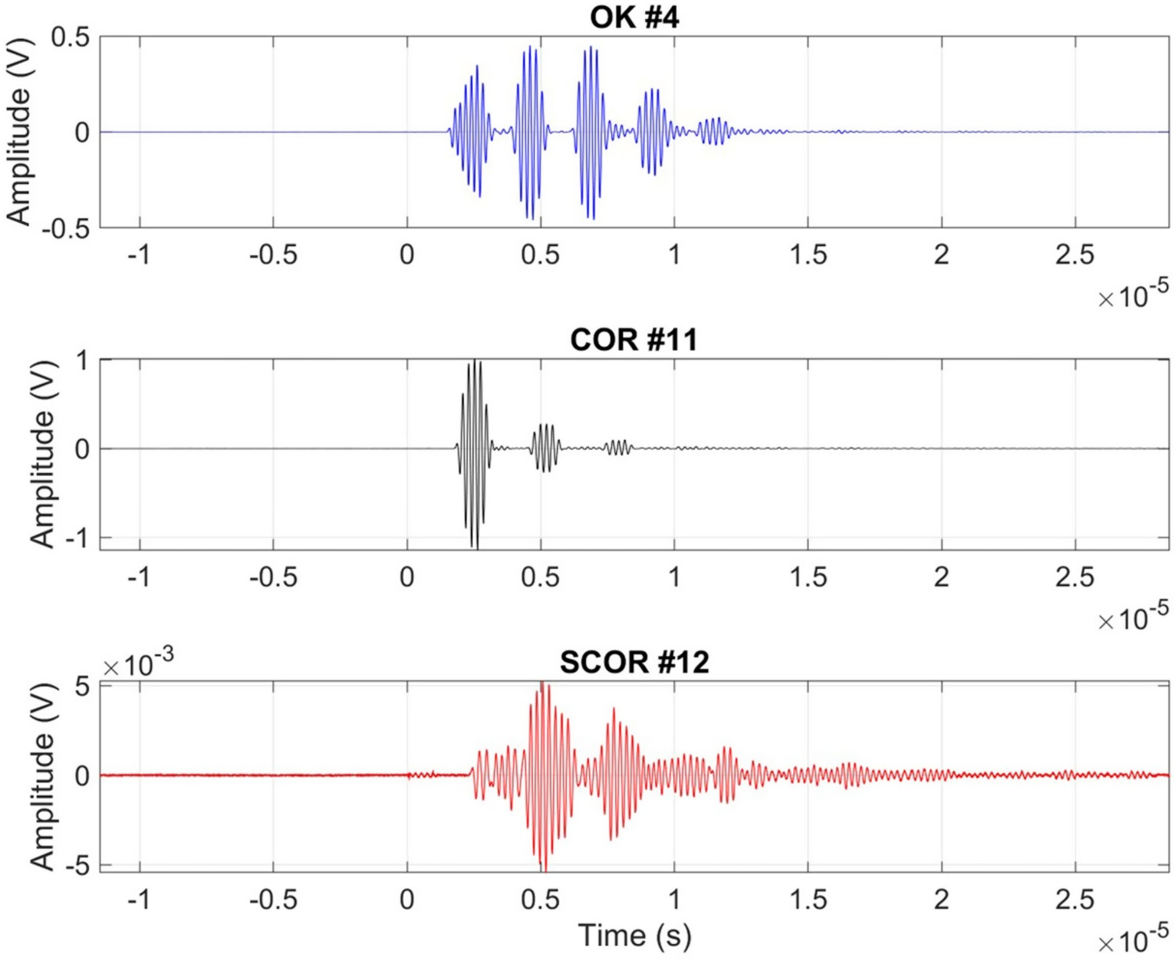

Figure 12. Received voltage signals at points OK #4 (upper), COR #11 (middle), and SCOR #12 (bottom). Voltage signals versus time acquired from the through-transmission measurements. The signals from points four and eleven indicate clear separation between echoes. The signal acquired at point twelve has no clear separation between echoes, indicating self-interaction.

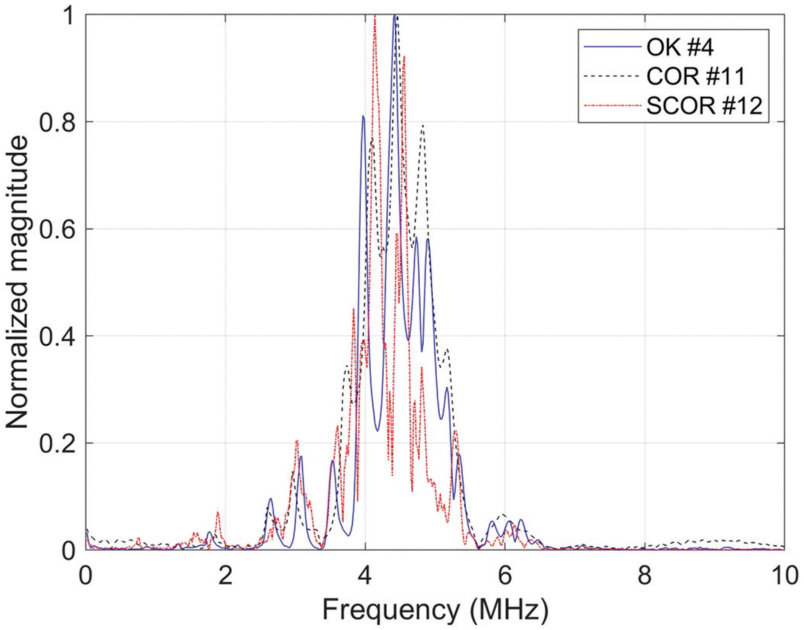

Figure 13. Normalised frequency spectra for the time signals at OK #4 (blue line), COR #11 (black dashed), and SCOR #12 (red dash-dotted).
Normalized spectra indicating that the weakest dominant peak to be around six percent of the strongest dominant peak.

are then self-normalised with respect to their maximum magnitude. The spectra are shown in Figure 13. The majority of energy is found in the detection bandwidth 0–10 MHz and is thus the band of main concern for the sideband analysis. By studying Figure 13, the dominant peaks, i.e. linear components, are found to be as weak as 6% of the maximum magnitude. This yields the maximum threshold of 0.06. The SPC (Figure 14 upper) is determined by Equation (5) with the threshold varying from >0 to 0.06 at steps of 0.005. It is evident that if Equation (5) is applied, the SPC will always start at 1 as the SPC is normalised for the total number of peaks for each measurement. In the present work, the SPC is instead normalised for the maximum number of peaks found at the reference region, and the same N_{tot} is used for all SPC computations. Here, this meant normalising by the total number of peaks acquired at OK#4. The SPC is shown to be consistently greater at the measurement points in the corroded regions compared to the non-corroded, especially at the lower thresholds. There is no significant difference in SPC between COR and SCOR, except at the minimum threshold.

As stated in Section 2.2, the level of nonlinearity might be better indicated by considering the energy contained in the sidebands relative to the energy in the excitation frequencies (dominant peaks), that is, the nonlinearity parameter α as given by Equation (6). The parameter is determined using the same data used in the SPC method. For comparative purposes, the α values were normalised with respect to the maximum parameter value found at OK#4. As seen in the lower part of Figure 14 there is a more clear separation between the regions and α is found to be more than twice as high at SCOR#12 compared to OK#4 at low threshold levels. Interestingly, although COR and SCOR had almost the same SPC, the α is significantly smaller for COR. Beyond the threshold level of 0.03, both COR and SCOR exhibit lower α and they approach 0 before OK does. This indicates that the weaker nonlinearity in the

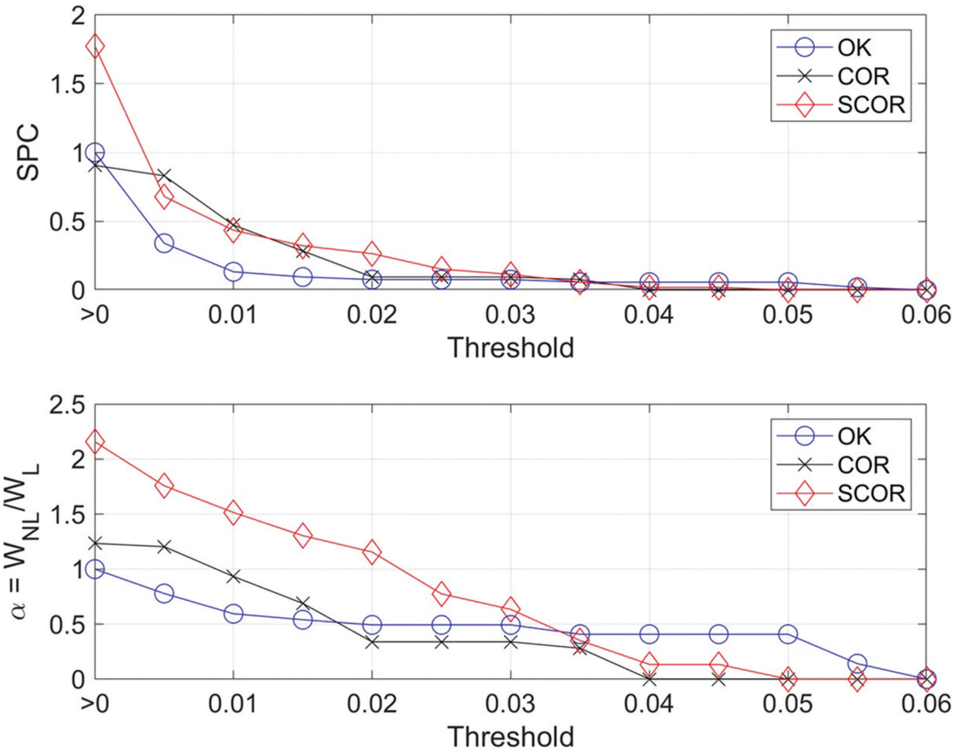

Figure 14. (Upper) SPC as a function of threshold varying from 0 to 0.06 of the maximum magnitude. (Lower) Parameter of nonlinearity α as a function of threshold normalised with respect to the maximum value for OK#4. Both parameters have been normalised by the respective maximum values found at point OK#4.
(Upper) The SPC graph shows that the greatest SPC at point twelve (SCOR) is approximately one and eight tenths times greater than the SPC at point four (OK). The corresponding SPC at point eleven is nine tenths of the SPC at point four. The SPC decreases exponentially until it reaches zero at the threshold value fifty-five tenths. (Lower) The α parameter value acquired at point twelve (SCOR) is two and two tenths greater than the corresponding value at point 4 (OK). The corresponding value at point eleven (COR) is one and two tenths greater than OK number four. The parameter value decreases in a linear fashion and reaches zero at the threshold value six tenths for OK, four tenths for COR, and five tenths for SCOR.

OK region causes the energy to be distributed to fewer frequency components, thus resulting in peaks with greater magnitudes but fewer sideband peaks in relation to those in the corroded regions. In the corroded regions, the energy is distributed to a greater number of frequencies and initially, the total energy contained in these peaks is greater than those at OK. As the threshold increases, the distributed energy is drastically reduced as the weaker but plentiful sidebands are ignored. Similarly, the uniformly corroded region COR had a similar SPC but the energy distributed to these peaks was lower than for SCOR. This indicates a clear step-wise increase in acoustical nonlinearity with an increasing grade of corrosion.

4.3. Comparing β', SPC, and a

Comparing the results gained from the pitch-catch measurements determining β' and those obtained from the transmission SPC and α measurements, it is found that the nonlinearity increases with increasing grade of corrosion. However, the increase is likely not as dramatic as indicated by β' in Figure 11(f)). Due to the difficulty of accurately extracting echoes from the measurements on SCOR measurement points, efforts were not made towards determining attenuation correction factors. It is assumed that if attenuation correction was applied in the pitch-catch measurements, the β' values at SCOR (and COR) would likely drop and perhaps indicate a similar trend as shown in the α distribution in Figure 14. Regardless, there are identifiable signal differences between the specimen regions which is significant for NDT purposes in real-life engineering applications such as the inspection of CLPs.

As shown in the micro- and tomographs in Figures 4 and 5 respectively, the SCOR-type corrosion product has several defects from microscopic ($10^{-6}m$) to macroscopic ($> 10^{-3}m$). This makes it very challenging to determine the exact source of nonlinearity as there might be many different contributing factors, some of which may be related to stress concentration at crack tips, and stiffness asymmetry. Moreover, the presence of large defects may decrease the measured nonlinearity, thus causing a weaker contrast between the inspected regions. This hypothesis cannot be confirmed by the present work due to its qualitative nature, however, previous quantitative research into damage evolution has indicated such trends [28].

It is clear that the inspected corroded regions have very rough surfaces. The effect of the roughness on the measured nonlinearity parameters are not entirely clear. Scattering causes greater attenuation, and mode conversions contribute to more complex effects possibly skewing the nonlinearity. There may be additional effects whose impact on the results are unknown. Previous research has indicated that roughness variations smaller than the probing wavelength in the coupling media may increase the observed nonlinearity [41]. However, it is has also been shown that rough surfaces may affect measurement reliability negatively [42]. The effects from roughness variations that are in the same order or greater than the probing wavelength in the coupling media is not clear. In addition to the cracks and delaminations found in corrosion products, it is suspected that roughness caused by corrosion affects the signal content. Thus, creating considerable signal differences between a smooth (non-corroded) and rough (corroded) surface. These differences may be utilised for NDE purposes. An evaluation of these effects is outside the scope of this paper, but greatly encouraged.

5. Conclusions

This study demonstrates that severe corrosion products with internal defects such as cracks and delaminations with sizes in the orders of magnitude from micro- to macroscopic can be detected and possibly localised using nonlinear ultrasound. Three parameters of acoustic nonlinearity were studied. The relative parameter of quadratic nonlinearity β' is given by the ratio between the second harmonic amplitude and the fundamental amplitude squared. This parameter was measured by using a pitch-catch setup, which is the most realistic setup for the inspection of a containment wall. The sideband peak count (SPC) is a measure of the number of sideband peaks generated by a wide band excitation. The parameter α describes the energy distributed in the nonlinear sideband components relative to the linear excitation components. The SPC measurements were based on through-transmission measurements to ensure that internal defects were excited. All three parameters indicated a significant increase in nonlinearity in the region containing the shell-type corrosion product with cracks and delaminations. The regular uniformly corroded region did not exhibit any significant increase in β', but both SPC and α indicated a small increase over the non-corroded region. Building upon these initial results, future work will investigate if the inherent nonlinearity caused by the heterogeneous nature of concrete will mask the nonlinearity from corroded plates. To this end, inspection of various concrete samples with embedded corroded steel plates will be carried out.

Acknowledgements

The sincerest gratitude is addressed to Associate Professor Monica Almqvist for granting access to the ultrasound lab and equipment at the Department of Biomedical Engineering at Lund University and for guidance during the work. We would also like to acknowledge the guidance from Professor Dmytro Orlov in operating the optical microscope at the division of Materials Engineering at Lund University. Last, but not least, gratitude is addressed to Dr. Sara Johansson at the division of Solid Mechanics at Lund University and the 4D imaging lab for the acquisition of X-ray tomography of the corrosion products presented in this paper.

Disclosure statement

The authors declare that they have no known competing financial interests or personal relationships that could have appeared to influence the work reported in this paper.

Funding

This work is supported by funding from The Swedish Energy Research Centre (Energiforsk BET165) and the Swedish Radiation Safety Authority (SSM2019-1114).

ORCID

Markus Nilsson http://orcid.org/0000-0002-6560-0029
Nils Rydén http://orcid.org/0000-0001-7138-2622

CRediT authorship contribution statement

Markus Nilsson: Conceptualisation, Methodology, Software, Investigation, Formal analysis, Visualisation, Writing – Original Draft, Writing – Review & Editing.
Peter Ulriksen: Conceptualisation, Supervision, Funding acquisition, Resources, Writing – Review & Editing.
Nils Rydén: Conceptualisation, Supervision, Writing – Review & Editing.

References

[1] Swedish Radiation Safety Authority. Nuclear power; 2022. Available from: https://www.stralsakerhetsmyndigheten.se/en/areas/nuclear-power/
[2] Paek Y, Kim S, Yoon E, et al. Introduction of Containment Liner Plate (CLP) corrosion. In: Transactions of the Korean nuclear society spring meeting. Jeju, Korea: Korean Nuclear Society; 2018. p. 17–19.

[3] Dunn D, Pulvirenti A, Klein P. Containment liner corrosion. Vol. 2, 15th International Conference on Environmental Degradation of Materials in Nuclear Power Systems-Water Reactors 2011 Colorado Springs, CO, USA; 2011. p. 985–996.

[4] Renshaw JB, Lhota JR, Muthu N, et al. Thermographic inspection of pipes, tanks, and containment liners. AIP Conf Proc. 2015;1650(April 2015):290–297.

[5] Tešić K, Baričević A, Serdar M. Non-Destructive corrosion inspection of reinforced concrete using ground-penetrating radar: a review. Materials. 2021;14(4):1–20.

[6] Michel A, Pease BJ, Geiker MR, et al. Monitoring reinforcement corrosion and corrosion-induced cracking using non-destructive x-ray attenuation measurements. Cement Concr Res. 2011;41(11):1085–1094. DOI:10.1016/j.cemconres.2011.06.006.

[7] Zaki A, Chai HK, Aggelis DG, et al. Non-Destructive evaluation for corrosion monitoring in concrete: a review and capability of acoustic emission technique. Sensors (Switzerland). 2015;15(8):19069–19101. DOI:10.3390/s150819069.

[8] Zhu W, Rose JL, Barshinger JN, et al. Ultrasonic guided wave NDT for hidden corrosion detection. Res Nondestr Eval. 1998;10(4):205–225. DOI:10.1080/09349849809409629.

[9] Zhao X, Gao H, Zhang G, et al. Active health monitoring of an aircraft wing with embedded piezoelectric sensor/actuator network: I. Defect detection, localization and growth monitoring. Smart Mater Struct. 2007;16(4):1208–1217. DOI:10.1088/0964-1726/16/4/032.

[10] Rudenko OV. Giant nonlinearities in structurally inhomogeneous media and the fundamentals of nonlinear acoustic diagnostic techniques. Phys Usp. 2006;49(1):69–87.

[11] Rudenko OV, Korobov AI, Izosimova MY. Nonlinearity of solids with micro- and nanodefects and characteristic features of its macroscopic manifestations. Acoust Phys. 2010;56 (2):151–157.

[12] Solodov I, Krohn N, Busse G. CAN: an example of nonclassical acoustic nonlinearity in solids. Ultrasonics. 2002;40(1–8):621–625.

[13] Jhang K-Y, Lissenden CJ, Solodov I, et al. Measurement of nonlinear ultrasonic characteristics. Singapore: Singapore Nature Singapore Pte Ltd; 2020.

[14] Matlack KH, Kim JY, Jacobs LJ, et al. Nonlinear Rayleigh waves to detect initial damage leading to stress corrosion cracking in carbon steel. AIP Conf Proc. 2012;1430 (31):1452–1459.

[15] Zeitvogel DT, Matlack KH, Kim JY, et al. Characterization of damage due to stress corrosion cracking in carbon steel using nonlinear surface acoustic waves. AIP Conf Proc. 2013;1511 (January 2013):1286–1293.

[16] Hogg SM, Anderson BE, Le Bas PY, et al. Nonlinear resonant ultrasound spectroscopy of stress corrosion cracking in stainless steel rods. NDT E Int. 2019;102 (October 2018):194–198. DOI:10.1016/j.ndteint.2018.12.007.

[17] Jiao J, Fan Z, Zhong F, et al. Application of ultrasonic methods for early detection of intergranular corrosion in austenitic stainless steel. Res Nondestr Eval. 2016;27 (4):193–203. DOI:10.1080/09349847.2015.1103922.

[18] Zhong F, Zhang C, Li W, et al. Nonlinear ultrasonic characterization of intergranular corrosion damage in super 304H steel tube. Anti-Corros Methods Mater. 2016;63 (2):145–152. DOI:10.1108/ACMM-05-2014-1390.

[19] Korenska M, Matysik M, Vyroubal P, et al. Assessment of reinforcement corrosion using nonlinear ultrasonic spectroscopy. NDT in Progress 2009 - 5th International Workshop of NDT Experts, Proceedings Prague, Czech Republic; 2009. p. 143–151.

[20] Antonaci P, Bruno CL, Scalerandi M, et al. Effects of corrosion on linear and nonlinear elastic properties of reinforced concrete. Cement Concr Res. 2013;51:96–103. DOI:10.1016/j.cemconres.2013.04.006.

[21] Climent MÁ, Miró M, Carbajo J, et al. Use of non-linear ultrasonic techniques to detect cracks due to steel corrosion in reinforced concrete structures. Materials. 2019;12(5):813. DOI:10.3390/ma12050813.

[22] Arumaikani T, Sasmal S, Kundu T. Detection of initiation of corrosion induced damage in concrete structures using nonlinear ultrasonic techniques. J Acoust Soc Am. 2022;151 (2):1341–1352.

[23] Féron D. Nuclear corrosion science and engineering. 22nd ed. Cambridge, UK: Woodhead Publishing Limited; 2012. p. 22.
[24] Kundu T, Eiras JN, Li W, et al. Fundamentals of nonlinear acoustical techniques and sideband peak count. In: Kundu T, editor. Nonlinear ultrasonic and vibro-acoustical techniques for nondestructive evaluation. Chapter 1. Cham, Switzerland: Springer Nature Switzerland; 2019. p. 1–88.
[25] Kundu T, editor. Nonlinear ultrasonic and Vibro-acoustical techniques for nondestructive evaluation. Cham, Switzerland: Springer Nature Switzerland AG; 2018.
[26] Nazarov VE, Sutin AM. Nonlinear elastic constants of solids with cracks. J Acoust Soc Am. 1997;102(6):3349–3354.
[27] Hedberg CM, Johnson E, Andersson SA, et al. Ultrasonic monitoring of a fiber reinforced plastic - Steel composite beam during fatigue. Vol. 2, Proceedings of the 6th European Workshop - Structural Health Monitoring 2012, EWSHM 2012 Dresden, Germany. 2012. p. 1254–1260.
[28] Donskoy D, Liu D. Vibro-Acoustic modulation baseline-free non-destructive testing. J Sound Vibr. 2021;492:115808. DOI:10.1016/j.jsv.2020.115808.
[29] Zaitsev VY. Nonlinear acoustics in studies of structural features of materials. MRS Bull. 2019;44(5):350–360.
[30] Kube CM, Arguelles AP. Ultrasonic harmonic generation from materials with up to cubic nonlinearity. J Acoust Soc Am. 2017;142(2):EL224–EL230. DOI:10.1121/1.4998139.
[31] Pantea C, Osterhoudt CF, Sinha DN. Determination of acoustical nonlinear parameter β of water using the finite amplitude method. Ultrasonics. 2013;53(5):1012–1019. DOI:10.1016/j.ultras.2013.01.008.
[32] Hafezi MH, Alebrahim R, Kundu T. Peri-Ultrasound for modeling linear and nonlinear ultrasonic response. Ultrasonics. 2017;80:47–57. DOI:10.1016/j.ultras.2017.04.015.
[33] Xu Y, Wang Q, Jiang X, et al. Nondestructive assessment of microcracks detection in cementitious materials based on nonlinear ultrasonic modulation technique. Constr Build Mater. 2021;267:121653. DOI:10.1016/j.conbuildmat.2020.121653.
[34] Chen XJ, Kim JY, Kurtis KE, et al. Characterization of progressive microcracking in Portland cement mortar using nonlinear ultrasonics. NDT E Int. 2008;41(2):112–118. DOI:10.1016/j.ndteint.2007.08.009.
[35] Neff D, Harnisch J, Beck M, et al. Morphology of corrosion products of steel in concrete under macro-cell and self-corrosion conditions. Mater Corros. 2011;62(9):861–871. DOI:10.1002/maco.201005861.
[36] Poupard O, L'Hostis V, Catinaud S, et al. Corrosion damage diagnosis of a reinforced concrete beam after 40 years natural exposure in marine environment. Cement Concr Res. 2006;36(3):504–520. DOI:10.1016/j.cemconres.2005.11.004.
[37] Köliö A, Honkanen M, Lahdensivu J, et al. Corrosion products of carbonation induced corrosion in existing reinforced concrete facades. Cement Concr Res. 2015;78:200–207. DOI:10.1016/j.cemconres.2015.07.009.
[38] Guyer RA, Johnson PA. Nonlinear mesoscopic elasticity: evidence for a new class of materials. Phys Today. 1999;52(4):30–36.
[39] Khodabandeloo B, Hedberg C, Berghuvud A. Resonance frequency measurements of a few materials for temperature variations resonance frequency measurements of a few materials for temperature variations analysis. Proceedings of the Baltic-Nordic Acoustic Meeting 2014 Tallinn, Estonia; 2014. June.
[40] Magda P, Stepinski T. Corrosion assessment using ultrasound. Diagnostyka. 2015;16(1):15–17.
[41] Yuan M, Dai A, Liao L, et al. Numerical study on surface roughness measurement based on nonlinear ultrasonics in through-transmission and pulse-echo modes. Materials. 2021;14(17):4855. DOI:10.3390/ma14174855.
[42] Chakrapani SK, Howard A, Barnard D. Influence of surface roughness on the measurement of acoustic nonlinearity parameter of solids using contact piezoelectric transducers. Ultrasonics. 2018;84:112–118. DOI:10.1016/j.ultras.2017.10.022.